





Article

Catalytic Hydrotreatment of Humins Waste over Bifunctional Pd-Based Zeolite Catalysts

Magdi El Fergani ¹, Natalia Candu ¹, Iunia Podolean ¹, Bogdan Cojocaru ¹, Adela Nicolaev ², Cristian M. Teodorescu ², Madalina Tudorache ¹, Vasile I. Parvulescu ¹ and Simona M. Coman ^{1,*}

¹ Department of Organic Chemistry, Biochemistry and Catalysis, Faculty of Chemistry, University of Bucharest, Bdul Regina Elisabeta 4-12, 030016 Bucharest, Romania

² National Institute of Materials Physics, Atomistilor 405b, 077125 Magurele-Ilfov, Romania

* Correspondence: simona.coman@chimie.unibuc.ro

Abstract: The catalytic hydrotreatment of humins, the solid byproduct produced from the conversion of C6 sugars (glucose, fructose) to 5-hydroxymethylfurfural (HMF), using supported Pd@zeolite (Beta, Y, and USY) catalysts with different amounts of Pd (i.e., 0.5, 1.0 and 1.5 wt%) was investigated under molecular hydrogen pressure. The highest conversion of humins (52.0%) was obtained on 1.5Pd@USY catalyst while the highest amount of humins oil (27.3%) was obtained in the presence of the 1Pd@Beta zeolite sample, at $P_{H_2} = 30$ bars and $T = 250$ °C. The major compounds in the humins oil evidenced by GC-MS are alcohols, organic acids, ethers, and alkyl-phenolics. However, although all these classes of compounds are obtained regardless of the nature of the catalyst used, the composition of the mixture differs from one catalyst to another. Furanic compounds were not identified in the reaction products. A possible explanation may be related to their high reactivity under the reaction conditions, in the presence of the Pd-based catalysts these compounds lead to alkyl phenolics, important intermediates in the petrochemical industry.

Keywords: palladium; zeolites; bifunctional catalysts; humins; hydrotreatment; biobased compounds



Citation: El Fergani, M.; Candu, N.; Podolean, I.; Cojocaru, B.; Nicolaev, A.; Teodorescu, C.M.; Tudorache, M.; Parvulescu, V.I.; Coman, S.M. Catalytic Hydrotreatment of Humins Waste over Bifunctional Pd-Based Zeolite Catalysts. *Catalysts* **2022**, *12*, 1202. <https://doi.org/10.3390/catal12101202>

Academic Editor: Roman Bulánek

Received: 31 July 2022

Accepted: 1 October 2022

Published: 9 October 2022

Publisher's Note: MDPI stays neutral with regard to jurisdictional claims in published maps and institutional affiliations.



Copyright: © 2022 by the authors. Licensee MDPI, Basel, Switzerland. This article is an open access article distributed under the terms and conditions of the Creative Commons Attribution (CC BY) license (<https://creativecommons.org/licenses/by/4.0/>).

1. Introduction

In the last number of decades, significant attention has been paid to the utilization of renewable biomass platform molecules as promising carbon resources that might partly be used as a substitute for fossil fuels. Furan-derivative compounds, for instance, are used in the production of a wide range of chemicals, including 2,5-dimethylfuran, furanedioic acid, pentanoic acid esters, levulinic acid (LA) and its esters, and γ -valerolactone [1,2]. However, due to their high reactivity, the furan-derivative compounds also tend to polymerize in the acid-catalyzed reactions, resulting in large amounts of undesirable polyfuranic polymer by-products (i.e., humins) which severely limit an efficient utilization of the renewable biomass [3,4]. To overcome this inconvenience, the formation of humins should be suppressed by developing efficient catalytic systems able to convert the biomass in a selective way to the targeted products. However, such an objective is difficult to achieve since the formation of humins is favored from the thermodynamic point of view. Alternatively, the humins formed during such processes should be valorized and several reports indicate their potential in the fabrication of materials such as composites [5], catalysts [6], or functional carbon materials [7].

The chemical structure of humins also recommends them as an important source for the production of chemicals. Thus, several reports already suggested humins as a proper feedstock for the production of important compounds such as hydrogen and synthesis gas [8], alkyl phenolics and oligomers (following a depolymerization and hydrodeoxygenation tandem) [9], easily transportable fuels with a high energy density or low molecular weight compounds (such as intermediates for the production of high added value bulk

chemicals like acetic and formic acids) [10]. In most of these approaches, the catalytic alternative provides important advantages [11–13].

However, in spite of its socio-economic importance, the valorization of humins via depolymerization and subsequent hydrodeoxygenation to liquid hydrocarbons is still in the infancy stage. In this context, Ru/C [9] and Pt/C [14] were reported as highly efficient catalysts for the liquefaction of humins, affording conversions of 60–70% at 400 °C, in the presence of isopropanol (IPA) as a hydrogen donor. Other studies carried out at the same temperature investigated the hydrodeoxygenation of fructose-derived humins in methanol, under H₂ (30 bars), taking Ru/C, Rh/C, Pt/C, and Pd/C as catalysts. Among these, the conversion reached 75% on Rh/C [15]. The replacement of C with supports such as TiO₂, ZrO₂, and CeO₂ led only to a small increase in conversion (around 80%) [16]. Very recent reports also indicated the high efficiency of a more complex Ru/W-P-Si-O bifunctional catalyst in the selective production of cyclic and aromatic hydrocarbons from humins under mild reaction conditions [17].

Inspired by this state of the art, the aim of this work was to develop an efficient catalytic system for the humins hydrodeoxygenation to functionalized low molecular mass organic molecules (such as alcohols, ketones, and phenolics) that may serve as a source for valuable bio-based chemicals. With this scope, the investigations focused on hierarchical tailored bifunctional Pd@zeolites (Beta, Y, and USY) with enhanced catalytic performances.

2. Results and Discussion

The structure of humins is still incompletely understood. However, for humins prepared from C6 sugars, the characterization studies indicated a core-shell morphology with a furan-rich structure containing ether and (hemi) acetal linkages [18–21]. The physico-chemical characterization of the synthesized humins [19] following a hydrothermal treatment of glucose indicated a chemical structure with a morphology in line with these literature studies [18,20,21]. It corresponded to spherical shell-core interconnected particles with a structure consisting of a furan-rich polymeric network linked by functionalized aliphatic chains with aldehyde and beta-hydroxyacids [19,21] (Figure 1).

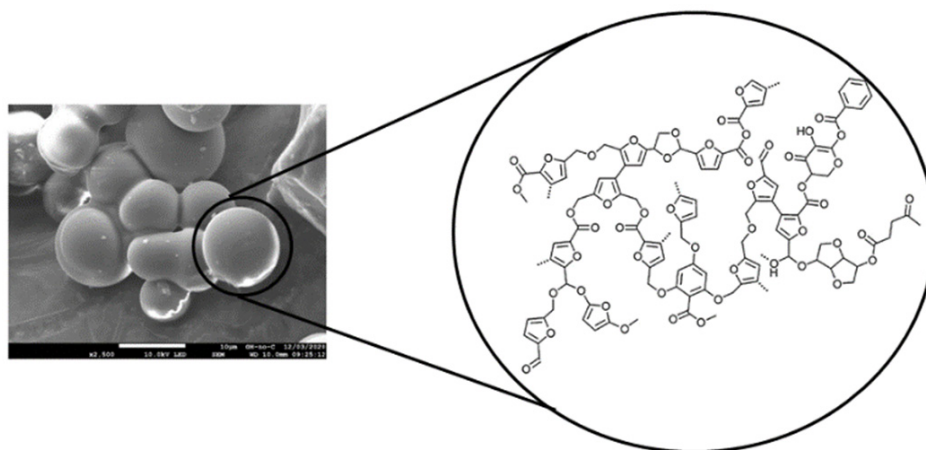


Figure 1. The morphology and molecular structure of humins obtained from C6 sugars (Adapted with permission from Ref [19,21], Elsevier, 2022).

2.1. Physico-Chemical Characterization of Pd@zeolite Catalysts

Zeolite-supported metal species are usually prepared via a simple impregnation approach [22,23]. However, the resulting catalysts are complex and this complexity is influenced by several factors, such as the zeolite framework, SiO₂/Al₂O₃ ratio, the type of exchanged cation, and the strength of the acid sites [24]. This work considered zeolites in the H-form with different SiO₂/Al₂O₃ ratios (i.e., 25.0 (H-Beta), 5.2 (H-Y), and 30.0 (H-USY)), and different textural properties.

N_2 adsorption-desorption isotherms of liquid nitrogen at $-196\text{ }^\circ\text{C}$ and the pore size distribution (determined from the BJH method) are shown in Figures 2 and 3, while the textural features of the prepared catalysts and supports (H-Beta, H-Y, and H-USY) are listed in Table 1.

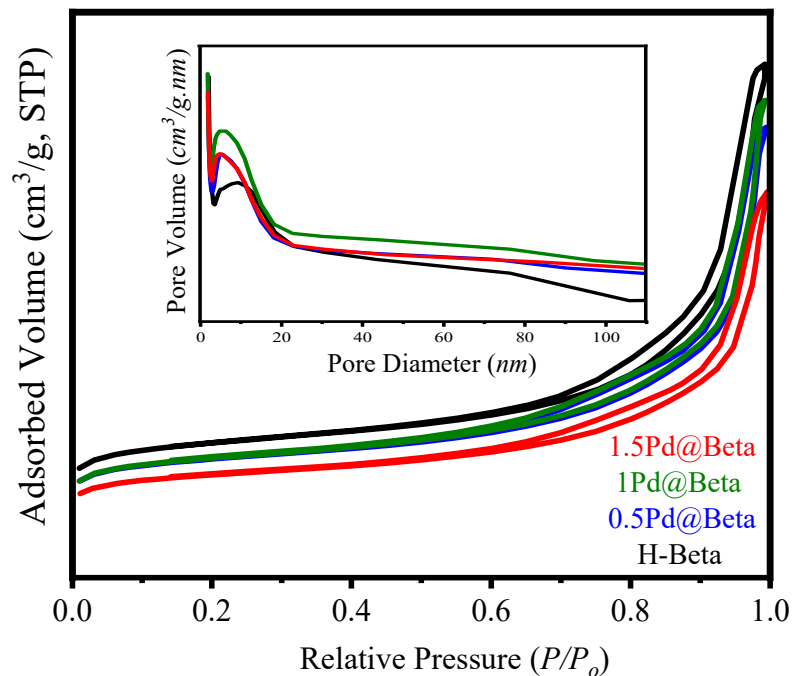


Figure 2. N_2 adsorption-desorption isotherms of the H-Beta, 0.5Pd@Beta, 1Pd@Beta, and 1.5Pd@Beta. The pore size distribution is given in the inset.

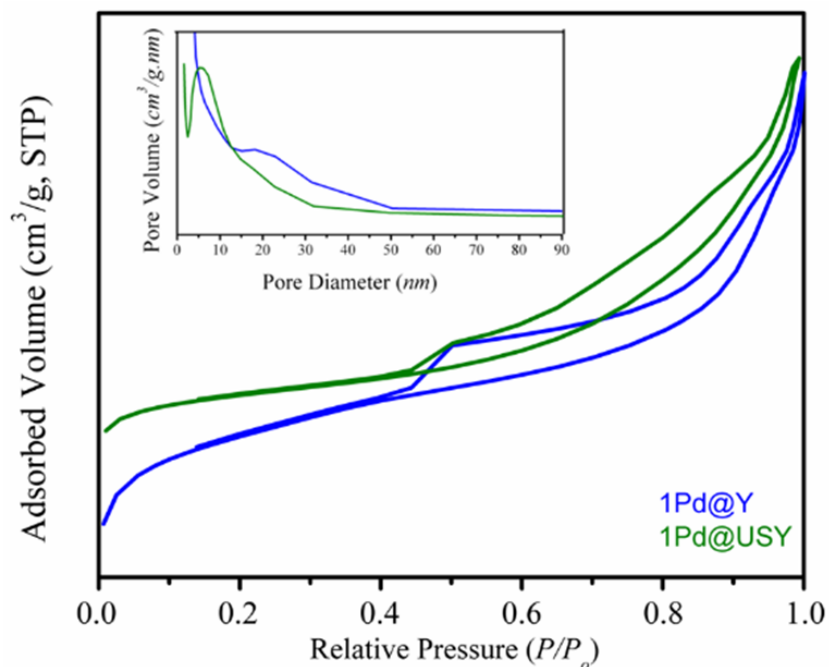


Figure 3. N_2 adsorption-desorption isotherms of the 1Pd@Y and 1Pd@USY samples. The pore size distribution is given in the inset.

Table 1. Physico-chemical characterization of the catalytic samples.

Entry	Catalyst	S_{BET} (m ² /g) ^a	S_{ext} (m ² /g) ^b	S_{micro} (m ² /g)	V_{total} (cm ³ /g) ^c	V_{meso} (cm ³ /g) ^d	V_{micro} (cm ³ /g) ^e
1	0.5Pd@Beta	500	177	323	0.65	0.50	0.15
2	1Pd@Beta	504	183	321	0.70	0.55	0.15
3	1.5Pd@Beta	433	153	280	0.56	0.43	0.13
4	1Pd@USY	668	174	494	0.45	0.22	0.23
5	1Pd@Y	352	79	273	0.31	0.18	0.13

^a—calculated by the BET method; ^b—external surface area calculated using the t-plot method; ^c—the total pore volume determined at a relative pressure (P/P_0) of 0.98; ^d—the mesopores volume calculated using the BJH method; ^e—the micropores volume calculated using the t-plot method.

The H-Beta zeolite supported catalysts presented Type IV isotherms, according to the IUPAC classification, and a H4 hysteresis loop at relatively pressures P/P_0 of 0.6–1.0 (Figure 2) with a bimodal micro-mesoporosity (Figure 2, inset). In accordance with previous works [25], the mesoporosity of Beta zeolite is the effect of the packing of small zeolite nanocrystals.

The Pd@Y and Pd@USY samples presented a combination of Type I and Type IV isotherms, with the appearance of a micropore filling at low relative pressures (i.e., <0.1) and a hysteresis loop at a relative pressure of 0.45–0.99. This indicates a hierarchical porous system combining micro- and mesoporosity. However, there are differences in the size of the pores, namely, 6.5 nm for 1Pd@Y and 20 nm for 1Pd@USY. The isotherms also showed a sharp rise in adsorbed amount near saturation (P/P_0 of 1.0) which is associated with condensation in the inter-particle voids (macropores). The presence of the macropores (cracks and voids) in the two CBV zeolites (i.e., H-Y CBV 600 and H-USY CBV 720) is caused by the steam and acid leaching treatments [26,27].

While the BET surface areas of Beta zeolite-based samples decreased from 680 m²/g for H-Beta, to 504–433 m²/g for Pd@Beta samples (Table 1, entries 1–3), the surface areas of Y- and USY-based catalysts decreased from 780 m²/g to 668 m²/g (1Pd@USY) and from 660 m²/g to 352 m²/g (1Pd@Y), respectively. The S_{micro} decrease paralleled S_{BET} values indicating some micropore blockages due to Pd deposition on the pore mouths during the reduction process [28,29].

The crystalline structure of the zeolite supports is well preserved after its impregnation with the palladium salt (Figures 4–6). In the case of Beta zeolite, the wider full widths at half-maxima of the diffraction peaks at 2θ of 7.79 and 22.53° (indicated with an asterisk in Figure 4) confirm the small crystal size of the employed Beta zeolite [30] and the existence of mesopores as an effect of their packing. The absence of the diffraction lines corresponding to the tetragonal PdO phase (i.e., 2θ angles at 33.6° (002), 42.0° (110), 54.9° (112), 60.3° (103), and 71.7° (211)) and/or metallic Pd (i.e., 2θ angles at 39.8° (111), 46.2° (200), 67.6° (220), and 81.4° (311) (JCPDS no. 46-1043)) [31] also indicates that the size of the PdO and Pd particles is small enough to not be detected by XRD, yielding a considerably high dispersion [29].

The chemical oxidation state of palladium, silicon, and aluminum was determined by XPS for the catalysts in the reduced form. The HR-XPS spectra are given in Figures S1–S4 and the spectral data in Tables S1–S3.

In all the samples, palladium mainly (80–83%) corresponds to a metallic Pd⁰ state (band located at 335.1–335.2 eV, Figures S1–S4 and Table S1) [32,33]. The difference of 16–19% is associated with PdO clusters (band located at 336.8–337.0 eV) [33,34].

The band corresponding to the Si2p level has been deconvoluted into two components (Figures S1–S4, Table S2) assigned to different ionic bonds [35]. For the Pd@USY catalyst, the main component at 102.5 eV (Table S2) corresponds to silicon in [SiO₄[−]] (i.e., 103.2 eV) in the vicinity of a distorted [AlO₄[−]] component [36] with different coordination numbers [35]. The band at higher binding energy (103.8–105.0 eV) is associated with [SiO₄[−]] components located in the proximity of the defected sites [33].

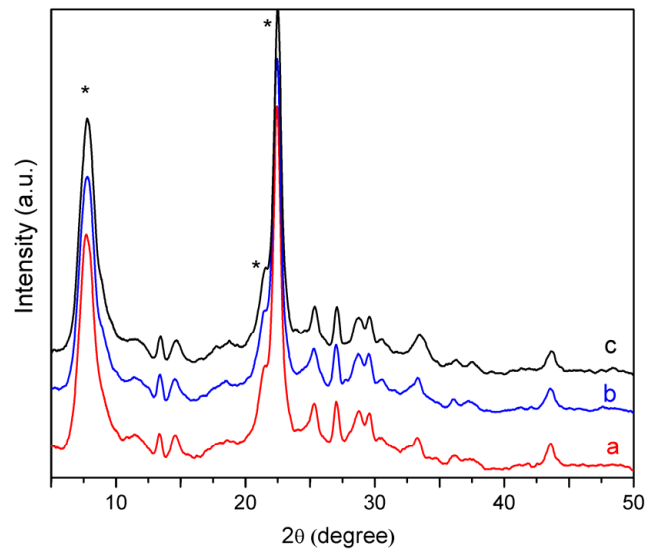


Figure 4. XRD patterns for Beta zeolite (a), 0.5Pd@Beta (b), and 1Pd@Beta (c) samples.

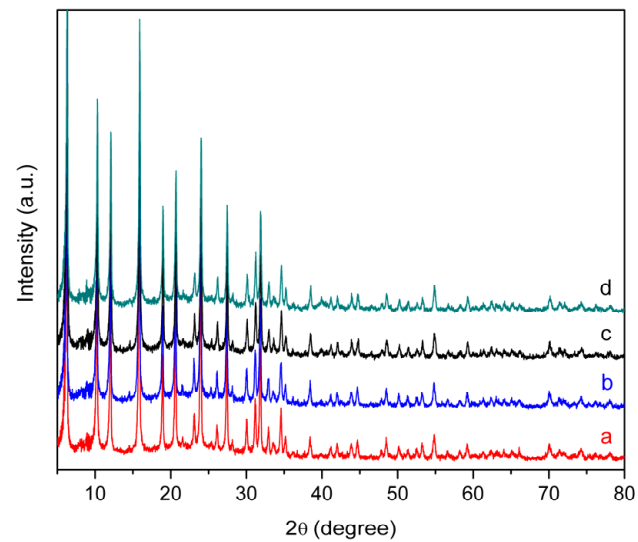


Figure 5. XRD patterns for H-Y zeolite (a), 0.5Pd@Y (b), 1Pd@Y (c), and 1.5Pd@Y (d) samples.

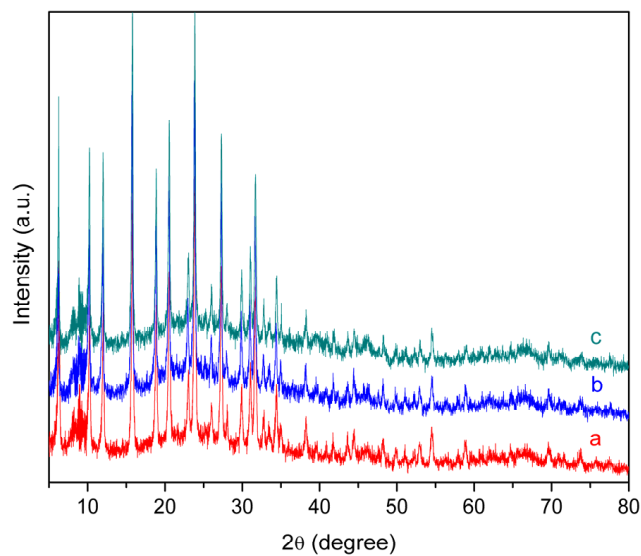


Figure 6. XRD patterns for H-USY zeolite (a), 0.5Pd@USY (b), and 1.5Pd@USY (c) samples.

Finally, the band associated with the Al 2p level has also been deconvoluted into two components located at 74.6–74.8 eV that were associated with aluminum in a III-fold state (Figures S1–S4, Table S3) and at 75.5–75.8 eV assigned to Al 2p in distorted $[\text{AlO}_4]^-$ units for Pd@Beta, and at 73.7–73.8 eV to Al 2p in IV- and VI-fold sites with or without a proton for Pd@Y and Pd@USY [33].

Table 2 compiles the atomic composition determined from the deconvolution normalized by taking the atomic sensitivity factors [37].

Table 2. The main elements and the atomic composition for each sample.

Sample	Si/Al Bulk	O 1s (%)	Si 2p (%)	Al 2p (%)	Si/Al XPS	Pd 3d5/2 (at%)	Pd ⁰ /Pd ⁿ⁺
1Pd@Beta	12.5	62.07	34.9	2.95	11.8	0.08	4.8
1.5Pd@Beta	12.5	62.38	34.82	2.66	13.1	0.14	4.1
1Pd@USY	15.0	59.49	30.00	10.39	2.9	0.11	4.6
1Pd@Y	2.6	63.58	35.11	1.23	28.5	0.07	5.1

For all the samples, the depletion of the palladium to aluminum ratio may confirm its agglomeration on the zeolite surface, most probably due to a micropore blockage. On the other hand, the reduction of the samples produced an enrichment of the surface in Al for Pd@USY, while for Pd@Y, a depletion of Al was observed. Aluminum enrichment of the surface for Pd@Y is accompanied by an increase in the defects in the $[\text{SiO}_4]^-$ zeolite framework (Table S2). For Pd@Beta, the surface Si/Al ratio is close to the bulk composition (Table 2).

Figures S5–S7 show the results of thermogravimetric and differential thermal (TG-DTA) analyses for the decomposition of palladium acetate deposited on zeolites, in a nitrogen atmosphere. The first loss of mass, accompanied by an endothermic peak below 100 °C, can be associated with the elimination of water from the zeolite channels while the second mass loss, accompanied by an exothermic effect at 280–330 °C, by the decomposition of palladium acetate [38]. However, as Figure S7 showed, the TG-DTA indicates a different decomposition profile of the Pd precursor. Along with the elimination of water, this is evidence of the other two decomposition steps of the palladium precursor (exothermic peaks at 230–240 °C and 440–460 °C, respectively), thus suggesting a different interaction with the zeolite carrier. As XRD and XPS analysis showed, for all the samples, the reduction step led to highly dispersed metallic Pd⁰ particles (preponderantly) and PdO clusters located in the depth of the carrier.

H₂-TPR allowed establishing the reducibility of the palladium species as an important element for the catalytic hydrotreatment of humins. The H₂-TPR profiles of the Pd@zeolites are displayed in Figure 7. In accordance with the literature, the consumed hydrogen corresponds to the reduction of PdO to metallic Pd [39].

As Figure 7 shows, the TPR profiles display at least two maxima at different temperatures, depending on the palladium loading and zeolite nature. The observed differences indicate the presence of different types of palladium species. For the case of Pd@Beta, the loading of palladium was higher, and the temperature corresponding to the H₂-TPR peak was higher, i.e., 235 °C (1.5Pd@Beta) > 180 °C (1Pd@Beta) > 160 °C (0.5Pd@Beta). Typically, such a variation indicates the formation of larger PdO nanoparticles for 1.5Pd@Beta and narrower particles for 0.5Pd@Beta, the former more difficult to reduce [40–43]. Indeed, the highest H₂ consumption was registered for the 0.5Pd@Beta (2.84 mmol/g) followed by 1Pd@Beta (0.74 mmol/g) and 1.5Pd@Beta (0.06 mmol/g). No H₂-TPR peak was observed at a low temperature (<100 °C) indicating a lack of PdO reduction in this range.

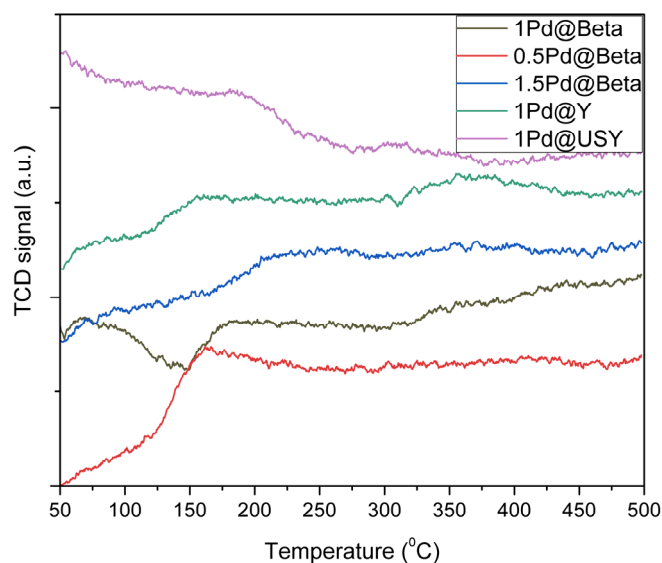


Figure 7. H₂-TPR profiles for Pd@zeolite samples.

On the other hand, for the same loading of palladium (i.e., 1 wt%) the TPR profiles indicate the presence of peaks at temperatures depending on the Si/Al ratio of the pristine zeolite. Therefore, the higher the content of aluminum in the zeolite framework, the lower the reduction temperature of the PdO particles, i.e., 190 °C (1Pd@USY, Si/Al = 15) > 180 °C (1Pd@Beta, Si/Al = 12.5) > 157 °C (1Pd@Y, Si/Al = 2.6), and the corresponding H₂ consumption: 0.91 mmol/g (1Pd@USY) > 0.74 mmol/g (1Pd@Beta) > 0.46 mmol/g (1Pd@Y). An additional peak in the TPR profiles has been determined in the range of 300–400 °C, which can be attributed to the presence of PdO nanoclusters inside the support micropores [40].

The DRIFT spectra collected for both non-calcined and the final catalysts (Figures 8–11) showed specific spectral characteristics (internal vibration of the framework TO₄ tetrahedron and vibration related to external linkages between tetrahedral units) of these zeolites [44]. All zeolites display a broad band in the 3000–3400 cm⁻¹ region attributed to the O–H stretching of hydrogen-bonded internal silanol groups and hydroxyl stretching of water, and a band at around 1630–1640 cm⁻¹ corresponding to the O–H bending mode of water. The bands in the 1017–722 cm⁻¹ range are attributed to the symmetric and asymmetric stretching vibrations of the Si–O–T linkages for TO₄ (T = Si and/or Al, respectively). Besides these, slight structural differences were detected through the asymmetry of the bands.

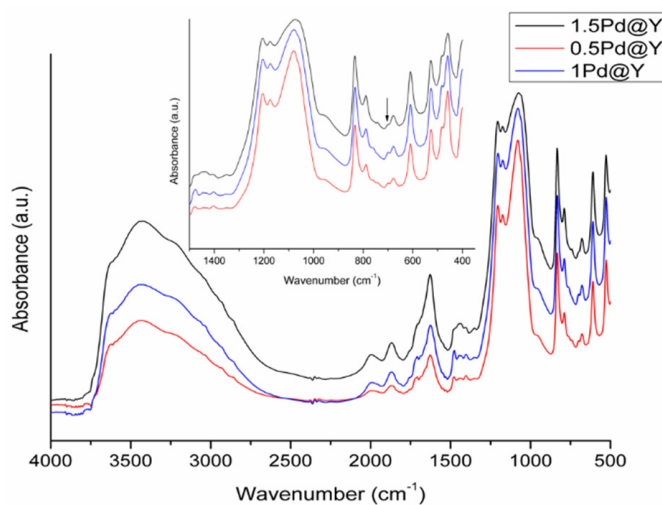


Figure 8. IR spectra of the non-calcined 0.5Pd@Y, 1Pd@Y, and 1.5Pd@Y samples and an inset in the 1500–400 cm⁻¹ range.

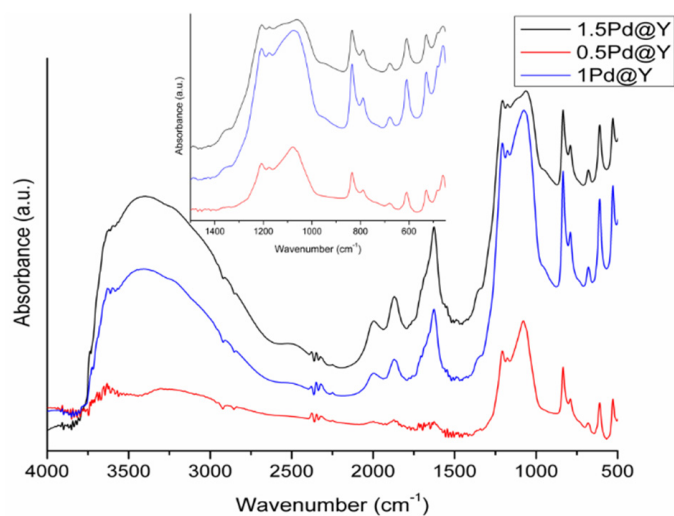


Figure 9. DRIFT spectra of the 0.5Pd@Y, 1Pd@Y, and 1.5Pd@Y and an inset in the 1500–400 cm⁻¹ range.

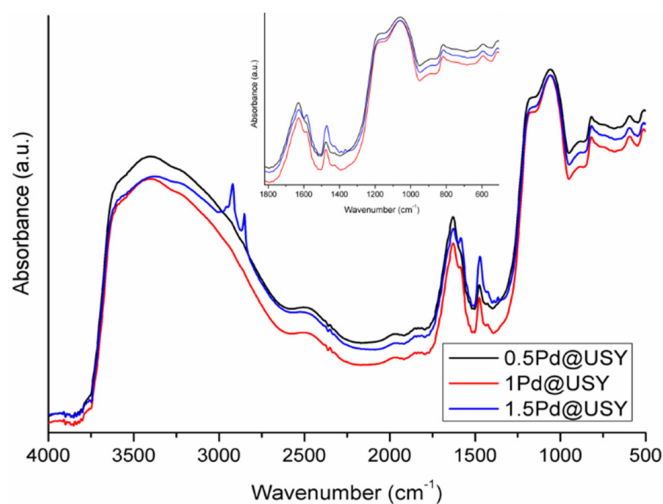


Figure 10. DRIFT spectra of the non-calcined 0.5Pd@USY, 1Pd@USY, and 1.5Pd@USY and an inset in the 1800–500 cm⁻¹ range.

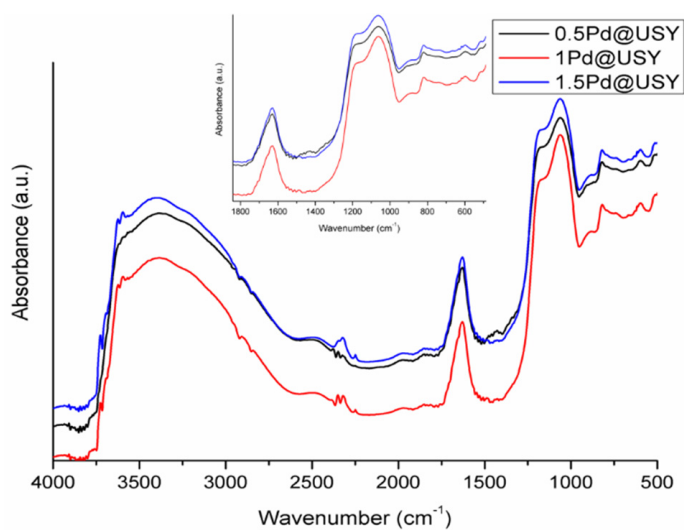


Figure 11. DRIFT spectra of the 0.5Pd@USY, 1Pd@USY, and 1.5Pd@USY and an inset in the 1800–500 cm⁻¹ range.

The DRIFT spectra for Pd@Y samples (Figures 8 and 9) display bands characteristic of Y zeolite [44]. The bands in the 1380–1530 cm^{-1} range are associated with the νCH_3 deformation. The $\nu\text{C-O}$ stretching vibrations of the Pd precursor are not visible in the DRIFT spectra of the final catalysts supporting its anchorage (Figure 9). In accordance with Banse and Koel [45], the disappearance of the band at 697 cm^{-1} , ascribed to the Pd–O bonds, also validates the formation of the metallic Pd nanoparticles (Figure 9).

H-Y materials typically display an acidic OH band in the vicinity of 3600 cm^{-1} [26]. Therefore, the two bands at 3600 and 3625 cm^{-1} are assigned to Si–O(H)–Al [25] or the OH groups located at the places left by the more easily removable framework aluminum atoms (Figure 9) [46].

For H-USY, the bands located at 1188, 1064, and 824 cm^{-1} (Figures 10 and 11) are characteristic of TO_4 tetrahedron units and are attributed to the external asymmetric, internal asymmetric, and external symmetric stretching vibrations of Si–O–T linkages (T = Si and/or Al) [47]. For non-calcined Pd@USY, the bands in the range of 1380–1530 cm^{-1} are associated with the νCH_3 deformation and $\nu\text{C-O}$ stretching vibrations from the Pd precursor. For the Pd@USY catalysts, these bands vanished due to the effect of the calcination and reduction steps. The broad absorption band in the region 3600–3200 cm^{-1} is assigned to the Si–OH groups interacting with each other through H-bonds. This large absorption band is also indicative of the high surface defectives. Additional bands were also registered at 3720 cm^{-1} and are most probably related to the presence of the Pd(II)–O–H groups (Figure 11) confirming the results of the XPS analysis.

As expected, the NH_3 -TPD analysis revealed the acidic properties of the Pd@zeolite catalysts (Figure 12 and Table 3). The NH_3 -TPD profiles (Figure 12) showed at least three maxima in the temperature ranges of 50–150, 150–250, and 250–400 $^\circ\text{C}$, respectively. The peaks in the region of 50–150 $^\circ\text{C}$ correspond to the weak adsorption of the ammonia molecules over the surface terminal silanols (Si–OH) [48] while those at 250–400 $^\circ\text{C}$ can be assigned to the surface Brønsted acid sites, namely, the bridged hydroxyl group (Si–OH–Al) [49]. The extra-framework Al species indicated by peaks in the 150–250 $^\circ\text{C}$ range behave as Lewis acid sites with a weaker strength than the bridged hydroxyl groups [49].

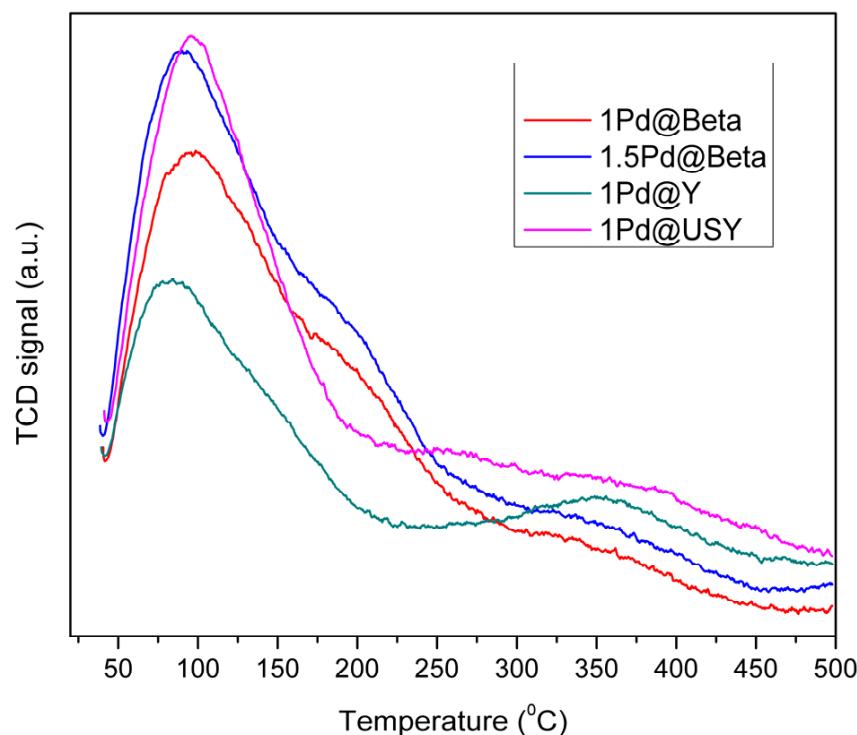


Figure 12. Temperature-programmed desorption profiles of ammonia for the investigated Pd@zeolites.

Table 3. Acid site concentration determined through NH₃-TPD measurements.

Catalyst	Acid Site Concentration ($\mu\text{mol NH}_3/\text{g}$)				L/B Ratio
	50–150 °C	150–250 °C	250–400 °C	Total	
H-Beta	66.0 (<300 °C)		4.0 (>300 °C)	70.0	-
0.5Pd@Beta	85.6	19.9	1.01	106.51	19.7
1Pd@Beta	91.51	20.08	1.81	113.40	11.1
1.5Pd@Beta	117.97	10.57	3.70	132.24	2.9
1 Pd@Y	54.27	-	14.92	69.19	0
1Pd@USY	110.49	0.12 (260 °C)	2.97	113.58	0.04

As Table 3 shows, for the Pd@Beta catalysts, the concentration of the surface Brønsted acid site (250–400 °C) decreased after the palladium deposition to a concentration of 1 wt%, most probably due to the Pd ion exchange which occurs with the replacement of the surface proton from Si–OH–Al. However, increasing the amount of the palladium from 1.0 wt% to 1.5 wt% led to an increase of the Brønsted acidity which, most probably, is related to the presence of the Pd(II)-O-H groups, also in accordance with XPS. In turn, the concentration of the Lewis acid sites (150–250 °C) increased greatly, most probably due to the presence of a high concentration of the well-dispersed PdO species. However, this effect is dependent on the palladium concentration and the nature of the zeolite. In accordance, if Pd@Beta samples registered with the highest concentrations of the Lewis acid sites decreased with the amount of palladium, for Pd@Y, the presence of the Lewis acidity (150–250 °C) is not detectable while for Pd@USY, although in a low concentration, is characterized by enhanced strength.

In summary, the characterization results suggest the presence of both oxide and metallic palladium species both on the outer surface of zeolite crystals (lower degree) and encapsulated within the channels or cavities of zeolites (preponderantly) [23]. During the calcination and reduction processes, the migration of palladium species in the zeolite micropores and their aggregation as larger particles take place. In the case of Beta zeolite, characterized by a large external surface, the higher the amount of palladium, the larger the formed particles and the lower the reduction degree. However, this process is also highly dependent on the zeolite framework [50], namely, a complex system of channels and micropores that can provide strong confinement effects and significantly inhibit particle growth to a particular size region. For a similar amount of palladium (i.e., 1 wt% Pd), the higher Si/Al ratio, the higher the reduction temperature and the higher the H₂ consumption, indicating a stronger interaction with the zeolite leading to small particles. In other words, the palladium dispersion is higher.

2.2. Catalytic Tests

Recently, Wang et al. [16] reported that in the presence of the supported noble metal catalysts, the hydrotreatment of humins in isopropanol (IPA) as a solvent at 400 °C led to aliphatic and aromatic hydrocarbons and phenolic compounds, alongside alcoholic and ketonic by-products (e.g., acetone and methyl isobutyl ketone (MIBK) most probably formed from the IPA solvent). In the presence of supported noble metals on carbon carriers (i.e., Ru/C, Rh/C, Pt/C, and Pd/C) under 30 bar H₂ at 400 °C, the main detected products are aromatic hydrocarbons, phenols, and esters [15].

In this work, the synthesized catalysts were screened for humins hydrotreatment in IPA as a solvent, at 250 °C, 30 bar H₂, and reaction times of 6, 12, and 24 h. In most of the reactions, 0.1 g humins and 10 mg catalyst were used (1:10 catalyst to humins mass ratio) but some experiments were also carried out taking 20 mg catalyst (1:5 catalyst to humins mass ratio). Under the reaction conditions, hydrogen can also be generated from the solvent (IPA) via catalytic transfer hydrogenation (CTH) [51,52] providing a larger amount of hydrogen needed in the reaction.

Figures 13 and 14 present the main results obtained in the presence of Pd@Beta and Pd@USY catalysts. After 6 h and with 10 mg of catalyst, the humins conversion was only

25% in the presence of 1Pd@Beta catalyst with a yield to humins oil below 10% (Figure 13). The conversion increased to 34% with the loading of palladium (i.e., 1.5%) but the yield in humins oil remained unchanged. A higher conversion of humins was accompanied by a higher yield in humins oil (20%) only after doubling the amount of catalyst from 10 mg to 20 mg. After 12 h, the conversion of humins increased from 23% (0.5Pd@Beta) to 33.7% (1Pd@Beta) and 43.1% (1.5Pd@Beta), for a catalyst to humins mass ratio of 1:10 (i.e., 10 mg of catalyst). The highest productivity in the humins oil (27.3%) was obtained in the presence of 1Pd@Beta, after 12 h. In the presence of the 1.5Pd@Beta catalyst, a maximum yield in the humins oil (but clearly inferior to that obtained in the presence of 1Pd@Beta catalyst) was obtained after 12 h; a prolonged reaction time of 24 h led to increased conversion of humins but an inferior yield of humins oil, suggesting the gasification of the oil with the increase of the reaction time.

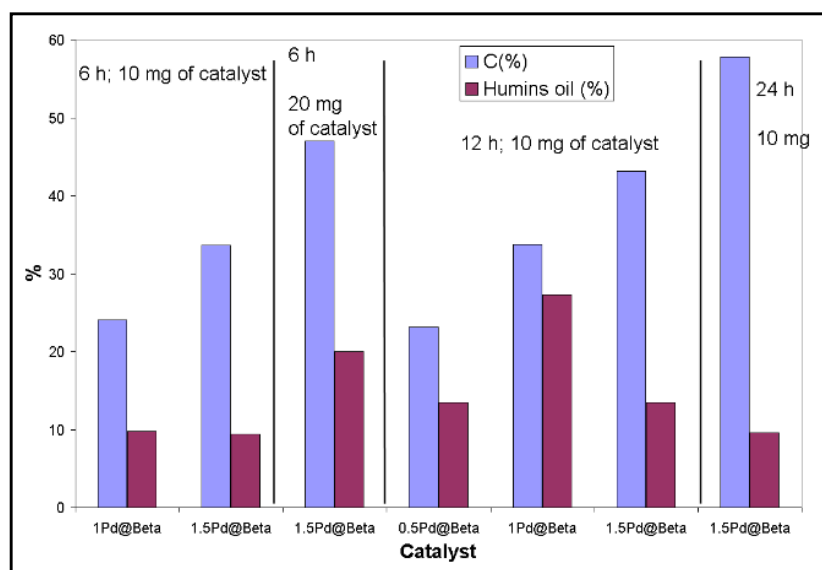


Figure 13. Catalytic performances of the Pd@Beta catalysts in the hydrodeoxygenation of humins (reaction conditions: 0.1 g humins, 8 mL IPA, 30 bars, T = 250 °C).

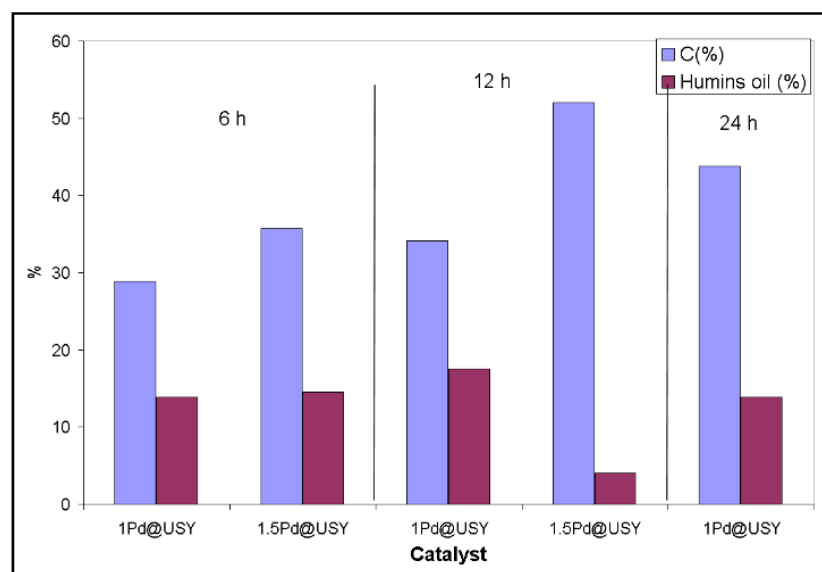


Figure 14. Catalytic performances of the Pd@USY catalysts in the hydrodeoxygenation of humins (reaction conditions: 0.1 g humins, 10 mg of catalyst, 8 mL IPA, 30 bars, T = 250 °C).

The nature of zeolite also exerts an influence on the conversion of humins and the yield of humins oil. Therefore, changing the support from Beta to USY zeolite, for the same concentration of palladium (i.e., 1.5%) and similar reaction conditions, led to an increase in the humins conversion from 43.1 to 52.0% (Figures 13 and 14). The textural properties of USY differ from that of Beta thus the catalytic active sites are possibly more easily accessible for rather large molecules for subsequent reactions.

For the series of USY-based-catalysts, the variation in the productivity of the humins oil showed a similar trend, i.e., higher amounts were obtained on the 1Pd@USY catalyst. However, in this case, these were significantly smaller (17.5%) than on 1Pd@Beta.

The lack of a correlation between these two efficiency parameters (i.e., humins conversion and humins oil yield) is, most probably, due to the formation of different quantities of gaseous compounds such as carbon dioxide and light hydrocarbons. Most probably, a higher loading of palladium (i.e., 1.5%) favors not only an enhanced conversion but also advanced depolymerization and hydrodeoxygenation to light hydrocarbons with decreased amounts of humins oil.

The average molecular weight (M_w) of untransformed humins fragments is broad, depending on the nature of the catalyst and the reaction conditions (Table 4). The product is a cocktail of molecules with different masses and PD values in the range of 1.5–3.2. It contains both low molecular weight and high molecular weight components that are not GC detectable.

Table 4. Molar masses of humins recovered from the hydrodeoxygenation reactions.

Entry	Catalyst	M_w (Da)	M_n (Da)	PD
1	1Pd@Beta	26,383	9600	2.7
2	1.5Pd@Beta	22,835	7195	3.2
3 ¹	1.5Pd@Beta	17,390	5923	2.9
4 ²	1.5Pd@Beta	11,312	3902	2.9
5 ³	1.5Pd@Beta	8370	4740	1.8
6	1Pd@USY	80,534	53,204	1.5
7	1.5Pd@USY	81,631	31,419	2.6

M_w —average molecular weight (Da); M_n —molecular mass obtained at half the height of the peak (Da); PD—dispersion factor. ¹—12 h, ²—24 h, ³—20 mg catalyst.

A typical GC-MS spectrum of the liquid phase is shown in Figure 15. Various products that belong to different organic product classes were observed. Among these products, the major ones are alcohols, hydroxy-acids, ketones, and alkyl-phenolics. An overview of the components identified by GC-MS analysis is given in Table 5. Alcohols are by far the most abundant compound class identified in humins oil, followed by hydroxy-acids and alkyl-phenolics. As humins contains significant amounts of furan units, the presence of furanic in the humins oil was expected. However, such compounds were not identified in the GC-MS analysis. A possible explanation may be related to the high reactivity of the furan-derived compounds under the reaction conditions (i.e., high temperatures and hydrogen pressures). In the presence of the Pd-based catalysts, these compounds can be transformed into alkyl-phenols.

Although all these classes of compounds are produced regardless of the nature of the catalyst, the composition of the mixture differed from one catalyst to another. Thus, an increased amount of the Pd in the catalyst formulation results in an enrichment of the humins oil in alkyl-phenolic compounds.

The results showed that the nature of the support and the palladium amount have a major effect on the conversion of the humins but also on the yield in the humins oil. A possible explanation may be related to the textural properties of the zeolites. These can greatly influence the accessibility of large molecules to the active metal sites and the subsequent reactions. Another effect can be induced by the different acid strengths of the investigated zeolites, which may initiate a repolymerization of reactive intermediates, i.e., an effect also observed in previous lignin depolymerization studies [53].

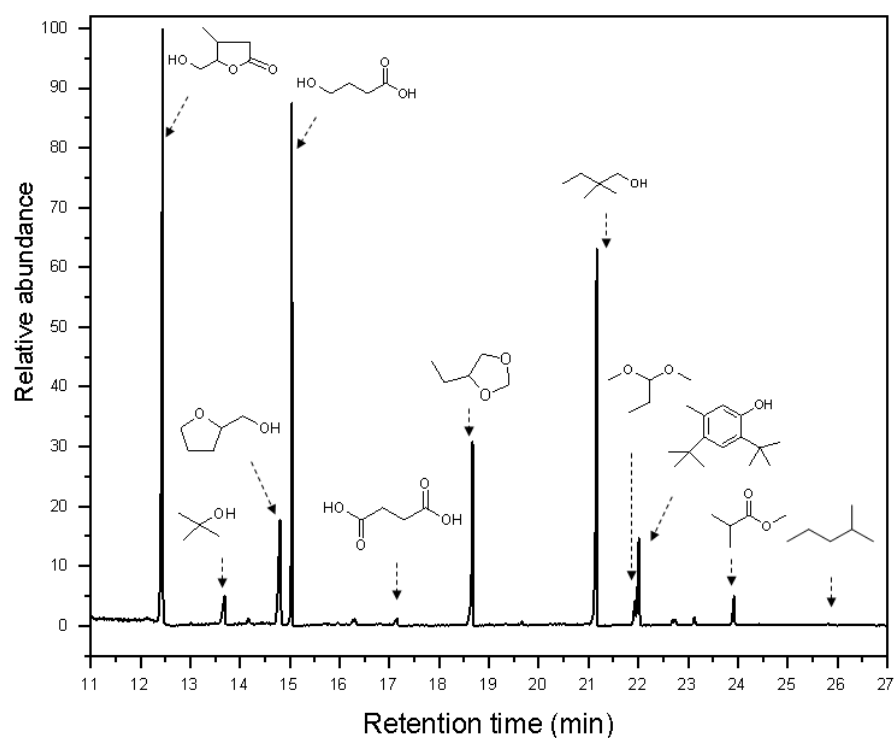
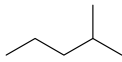
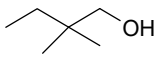
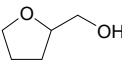
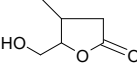
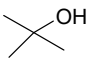
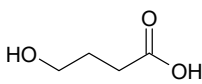
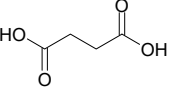
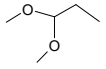
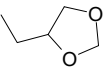
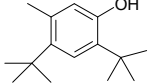
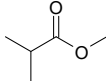


Figure 15. GC-MS spectrum of the humins oil (from the hydrodeoxygenation reaction in the presence of 1.5Pt@USY, at 250 °C, 6 h, and 30 bar of H₂).

Table 5. Major component classes and representative individual components in the liquid phase analysis by GC-MS.

Alkanes	 2-methyl-pentane
Alcohols	 2,2-dimethylbutanol  tetrahydro-furfurylalcohol  4-hydroxy-5-(hydroxymethyl)oxolan-2-one  1,1-dimethyl ethanol
Acids	 4-hydroxybutanoic acid  butanedioic acid
Esters	 1,1-dimethoxypropane  4-ethyl-1,3-dioxolane
Phenolics	 4,6-di-tert-butyl-m-cresol
Esters	 methyl isobutyrate

3. Materials and Methods

3.1. Humins Synthesis and Characterization

Humins were prepared in accordance with a recently reported hydrothermal methodology [19]. An aqueous solution containing D-glucose (36.0 g D-glucose in 200 mL water, 1.0 M) and H₂SO₄ (1.078 g, 5.5 mM) was added to an autoclave and heated at 180 °C, for 7 h. The solid (i.e., humins) was isolated by filtration and washed with an excess of water (300 mL), dried for 12 h at 80 °C, grounded, and purified via a Soxhlet extraction.

3.2. Synthesis of Bi-Functional Pd@zeolite Catalysts

Zeolites (purchased from ZEOLYST International Company) in this study had a SiO₂/Al₂O₃ ratio of 25.0 (NH₃-Beta CP814E), 5.2 (H-Y CBV 600), and 30.0 (H-USY CBV 720), respectively. The surface areas of the zeolites, provided by the company are 680 m²/g (CP814E), 660 m²/g (CBV 600), and 780 m²/g (CBV 720) [54]. Before use, the NH₃-Beta zeolite was calcined in an oven at 450 °C, static air atmosphere, for 10 h, when NH₄⁺ was decomposed to NH₃(g) and H⁺, generating the H-Beta zeolite. The calcination temperature was raised with a temperature ramp of 2 °C/min. The other zeolites were dried in a vacuum for 6 h at 110 °C. The preparation of the catalysts was performed as follows: over 1.5 g zeolite was added to a solution containing 16.0, 32.0, or 48.0 mg Pd(CH₃COO)₂ (for a final content of 0.5 wt% Pd, 1.0 wt% Pd and 1.5 wt% Pd, respectively) in benzene (15 mL). The mixture was stirred for 24 h at room temperature, after which the solvent was removed by evaporation. The obtained solids were dried at 80 °C for 8 h, calcined at 500 °C for 4 h (heating rate 1 °C/min), and reduced in a stream of hydrogen (flow rate of 30 mL/min) at 400 °C, for 4 h (heating rate 5 °C/min). The final catalysts were denoted as: 0.5Pd@Beta, 1Pd@Beta, 1.5Pd@Beta, 0.5Pd@Y, 1Pd@Y, 1.5Pd@Y, 0.5Pd@USY, 1Pd@USY, and 1.5Pd@USY.

3.3. Pd@zeolite Catalysts Characterization

The synthesized catalysts were characterized by various techniques such as adsorption-desorption isotherms of nitrogen at −196 °C, X-ray diffraction (XRD), thermogravimetry (TG-DTA), diffuse reflectance infrared Fourier transform spectroscopy (DRIFT), temperature programmed desorption (CO₂- and NH₃-TPD), temperature programmed reduction (H₂-TPR) and X-ray photoelectron spectroscopy (XPS).

The textural properties were determined from nitrogen adsorption-desorption isotherms of nitrogen at −196 °C using a Micrometrics Tristar 3020 apparatus. Prior to adsorption, all samples were systematically degassed at 200 °C under primary vacuum for 4 h. The surface area was calculated from the BET equation and the pore size distribution was determined based on the Barret-Joyner-Halenda (BJH) approach.

XRD diffractograms were recorded with a Schimadzu XRD-7000 diffractometer with K α radiation ($\lambda = 1.5418 \text{ \AA}$, 40 kV, 40 mA) with steps of 0.02° in the 2 θ range of 5–80 degrees.

TG-DTA analyses were performed with a Shimadzu apparatus. The heating rate of the sample was maintained at a value of 10 °C min^{−1}, starting from room temperature up to 800 °C, in a nitrogen stream of 10 mL min^{−1}.

DRIFT spectra were recorded with a Thermo Electron Nicolet 4700 FTIR spectrometer equipped with a Smart accessory for diffuse reflectance measurements. IR spectra were scanned in the range of 4000–400 cm^{−1}. The final spectra corresponded to an accumulation of 400 scans. The baseline was collected taking KBr as reference.

NH₃-TPD experiments were carried out in an AutoChem II 2920 station from Micromeritics. The samples, placed in a U-shaped quartz reactor with an inner diameter of 0.5 cm, were pretreated under He (Purity 5.0, from Linde) at 120 °C for 1 h and then exposed to a flow of NH₃ (10.01% in He, SIAD) for 1 h. After that, the samples were purged with a flow of He (50 mL·min^{−1}) for 30 min at 25 °C in order to remove the weakly adsorbed species. TPD was then started, with a heating rate of 3 °C·min^{−1} till 500 °C. The desorbed products were analyzed with a TC detector/by GC-TCD chromatography. The desorbed NH₃ expressed as μmol s per gram of catalyst was determined using a calibration curve.

H₂-TPR was performed in the same station. The samples were kept under a flow of H₂ (5% in He) with a heating rate of 3 °C·min⁻¹ till 500 °C. The consumed H₂ was detected by a thermo-conductivity detector (TCD) and expressed as mmols per gram of catalyst.

The X-ray photoelectron spectroscopy (XPS) analysis of the samples was performed in an AXIS Ultra DLD (Kratos Surface Analysis) setup using Mg K α (1253.6 eV) radiation produced by a non-monochromatized X-Ray source at operating power of 144 W (12 kV \times 12 mA). The base pressure in the analysis chamber was at least 1 \times 10⁻⁸ mbar. All core level spectra were deconvoluted with the use of Voigt functions (Lorentzian and Gaussian widths) with a distinct inelastic background for each component [55,56]. A minimum number of components is used to obtain a convenient fit. The binding energy scale was calibrated to the C 1 s standard value of 284.6 eV (measured at the beginning of XPS spectra).

3.4. Catalytic Tests

Catalytic tests (i.e., humins depolymerization followed by hydrodeoxygenation reactions) were performed under the following conditions: 0.01–0.02 g of catalyst was added to a solution of 0.1 g humins in 8 mL of isopropanol (IPA). After closing the autoclave, it was pressurized with 30 bars of molecular hydrogen and the mixture was heated at 250 °C, under stirring, for 6–24 h. After the reaction, the reactor was cooled to room temperature, the pressure was released, the catalyst and the untransformed humins were separated by filtration, and the collected reaction products from the liquid phase were recovered by vacuum distillation of the solvent. The reaction liquid product was denoted as “*humins oil*”. The solid residue (unreacted humins and catalyst) was dried at 70 °C for 12 h, under vacuum, and weighed for mass balance calculations. Solid and liquid yields were calculated on the base of the formula:

$$\text{Solid yield (\%)} = \frac{\text{mass of solid product} - \text{catalyst intake}}{\text{humins intake}} \times 100$$

$$\text{Liquid yield (\%)} = \frac{\text{mass of liquid phase}}{\text{humins intake} + \text{solvent intake}} \times 100$$

The conversion was calculated based on humins intake and the solid products isolated after the reaction. It assumes that the solid residue consists of unconverted humins and, as such, the solid form due to repolymerization reactions of reactive intermediates was not taken into account.

$$\begin{aligned} \text{Humins conversion (\%)} \\ = \frac{\text{humins intake} - (\text{mass of solid after reaction} - \text{catalyst intake})}{\text{humins intake}} \times 100 \end{aligned}$$

3.5. Products Analysis

The obtained products (i.e., humins oil) were analyzed by GC-FID chromatography (GC-Shimadzu) and identified by GC-MS analysis (THERMO Electron Corporation equipped with TG-5SilMS column, 30 m \times 0.25 mm \times 0.25 μ m). The non-transformed humins were analyzed by GPC-SEC chromatography to reveal its degree of decomposition during the catalytic process. An Agilent Technologies instrument (model 1260) equipped with Agilent PLgel MIXED-E column (7.5 \times 300 mm, 3 μ m) and a multi-detection unit (260 GPC/SEC MDS with RID, LS, and vs. detectors) was used in this scope. The analyses were performed under the following conditions: THF flow—1 mL/min, injection volume—100 μ L, and temperature 35 °C. Calibration of the GPC system was performed in the range of 162–1,000,000 g mol⁻¹, with good accuracy of measurements for MW > 1000. GPC chromatograms allowed the calculation of the average molecular weight of the humins fragments recovered from the hydrodeoxygenation reaction.

4. Conclusions

In conclusion, a series of Pd@zeolite catalysts with loadings of 0.5 wt%, 1.0 wt% and 1.5 wt% Pd (zeolites: Beta (Si/Al = 12.5), Y (Si/Al = 2.6) and USY (Si/Al = 15)) were prepared using palladium acetate ($\text{Pd}(\text{CH}_3\text{COO})_2$) as a precursor.

The resulting catalysts were characterized by XRD, adsorption-desorption isotherms of nitrogen, XPS, TG-DTA, H_2 -TPR, DRIFT, and NH_3 -TPD techniques. The obtained results suggest the formation of the hierarchically micro-mesoporous architectures in which both oxide and metallic palladium species exist preponderantly encapsulated within the channels or cavities of zeolites. During the activation (i.e., calcination and reduction) process the migration of palladium species and their aggregation as larger particles take place. The higher the amount of palladium, the larger the formed particles and the lower the reduction degree. On the other hand, the higher the Si/Al ratio, the stronger interaction of the palladium species with the zeolite framework. This leads to small particles highly dispersed on the zeolite surface.

The humins obtained from glucose were converted by hydrodeoxygenation to humins oil using the prepared Pd@zeolite catalysts, at only 250 °C. In the series of Beta-based catalysts, the highest level of conversion was 57.8% (1.5Pd@Beta, 24 h, 250 °C) while the highest percentage in the humins oil was 27.3%, on the 1Pd@Beta catalyst (12 h, 250 °C). For the series of USY-based-catalysts, the variation in the productivity of the humins oil showed a similar trend, i.e., higher amounts were obtained on the 1Pd@USY catalyst. However, in this case, these were significantly smaller (17.5%) than on 1Pd@Beta. Unfortunately, for high humins conversions, the amount of humins oil is lower. These results clearly show a high influence of the features of the catalyst (nature of the Pd species and physico-chemical features of the zeolite carrier) upon the reaction products.

These findings confirm that the solid useless humins waste may be (partly) depolymerized to liquid oil, which may further serve as a source for the production of valuable biobased chemicals such as alcohols, hydroxyacids, ketones, and alkyl-phenolics. The advantage of the process consists of a much lower reaction temperature by comparing with those reported in the literature (250 °C versus 400 °C). However, increased productivity of the process requires additional investigations focusing on the optimization of the catalytic system.

Supplementary Materials: The following supporting information can be downloaded at: <https://www.mdpi.com/article/10.3390/catal12101202/s1>, Figure S1: Deconvolutions of the HR XPS spectra for sample 1Pd@Y and the survey spectra; Figure S2: Deconvolutions of the HR XPS spectra for sample 1Pd@Beta and the survey spectra; Figure S3: Deconvolutions of the HR XPS spectra for sample 1.5Pd@Beta and the survey spectra; Figure S4: Deconvolutions of the HR XPS spectra for sample 1Pd@USY and the survey spectra; Figure S5: TG-DTA profiles of 0.5Pd@Beta (A) and 1Pd@Beta (B); Figure S6: TG-DTA profiles of 0.5Pd@Y (A) and 1.5Pd@Y (B); Figure S7: TG-DTA profiles of 0.5Pd@USY (A), 1Pd@USY (B) and 1.5Pd@USY (C); Table S1: Binding energies and the fractions of the $\text{Pd}_{3d5/2}$; Table S2: Si 2p peak components of Pd@zeolites samples; Table S3: Al 2p peak components of the Pd@Zeolite samples.

Author Contributions: Conceptualization, S.M.C.; methodology, N.C., M.E.F. and I.P.; validation, M.T., C.M.T., A.N. and B.C.; formal analysis, M.T., B.C., A.N. and N.C.; investigation, N.C., M.E.F., A.N. and I.P.; writing—original draft preparation, S.M.C.; writing review and editing, S.M.C. and V.I.P.; visualization, S.M.C. and V.I.P.; supervision, S.M.C., C.M.T. and V.I.P.; funding acquisition, N.C. All authors have read and agreed to the published version of the manuscript.

Funding: This study was funded by the Government of Romania, Ministry of Research and Innovation, project PN-III-P1-1.1-TE-2019-1933, Nr.69/2020.

Conflicts of Interest: The authors declare no conflict of interest.

References

1. Jing, Y.; Guo, Y.; Xia, Q.; Liu, X.; Wang, Y. Catalytic production of value-Added chemicals and liquid fuels from lignocellulosic biomass. *Chem* **2019**, *5*, 2520–2546. [[CrossRef](#)]
2. Covinich, L.G.; Clauser, N.M.; Felissia, F.E.; Vallejos, M.E.; Area, M.C. The challenge of converting biomass polysaccharides into levulinic acid through heterogeneous catalytic processes. *Biofuels Bioprod. Biorefin.* **2020**, *14*, 417–444. [[CrossRef](#)]
3. Ding, D.; Wang, J.; Xi, J.; Liu, X.; Lu, G.; Wang, Y. High-yield production of levulinic acid from cellulose and its upgrading to γ -valerolactone. *Green Chem.* **2014**, *16*, 3846–3853. [[CrossRef](#)]
4. Ding, D.; Xi, J.; Wang, J.; Liu, X.; Lu, G.; Wang, Y. Production of methyl levulinate from cellulose: Selectivity and mechanism study. *Green Chem.* **2015**, *17*, 4037–4044. [[CrossRef](#)]
5. Mija, A.; van der Waal, J.C.; Pin, J.M.; Guigo, N.; de Jong, E. Humins as promising material for producing sustainable carbohydrate-derived building materials. *Constr. Build. Mater.* **2017**, *139*, 594–601. [[CrossRef](#)]
6. Sukanuma, S.; Nakajima, K.; Kitano, M.; Yamaguchi, D.; Kato, H.; Hayashi, S.; Hara, M. Hydrolysis of cellulose by amorphous carbon bearing SO₃H, COOH, and OH Groups. *J. Am. Chem. Soc.* **2008**, *130*, 12787–12793. [[CrossRef](#)]
7. Pye, E.K. Lignin Line and Lignin-Based Product Family Trees. In *Biorefineries-Industrial Processes and Products*; Kamm, B., Gruber, P.R., Kamm, M., Eds.; Wiley-VCH Verlag GmbH: Weinheim, Germany, 2008; Volume 2, pp. 165–199.
8. Hoang, T.M.C.; Eck, E.R.H.V.; Bula, W.P.; Gardeniers, J.G.E.; Lefferts, L.; Seshan, K. Humins based by-products from biomass processing as a potential carbonaceous source for synthesis gas production. *Green Chem.* **2015**, *17*, 959–972. [[CrossRef](#)]
9. Wang, Y.; Agarwal, S.; Kloekhorst, A.; Heeres, H.J. Catalytic hydrotreatment of humins in mixtures of formic acid/2-Propanol with supported ruthenium catalysts. *ChemSusChem* **2016**, *9*, 951–961. [[CrossRef](#)]
10. Agarwal, S.; Es, D.V.; Heeres, H.J. Catalytic pyrolysis of recalcitrant, insoluble humin byproducts from C₆ sugar biorefineries. *J. Anal. Appl. Pyrol.* **2017**, *123*, 134–143. [[CrossRef](#)]
11. Sangregorio, A.; Guigo, N.; Waal, J.C.V.N.; Sbirrazzuoli, N. Humins from biorefineries as thermoreactive macromolecular systems. *ChemSusChem* **2018**, *11*, 4246–4255. [[CrossRef](#)]
12. Hoang, T.M.C.; Lefferts, L.; Seshan, K. Valorization of humin-based byproducts from biomass processing—A route to sustainable hydrogen. *ChemSusChem* **2013**, *6*, 1651–1658. [[CrossRef](#)]
13. Maerten, S.G.; Voß, D.; Liauw, M.A.; Albert, J. Selective catalytic oxidation of humins to low-chain carboxylic acids with tailor-made polyoxometalate catalysts. *ChemistrySelect* **2017**, *2*, 7296–7302. [[CrossRef](#)]
14. Wang, Y.; Agarwal, S.; Heeres, H.J. Catalytic liquefaction of humin substances from sugar biorefineries with Pt/C in 2-Propanol. *ACS Sustain. Chem. Eng.* **2017**, *5*, 469–480. [[CrossRef](#)]
15. Cheng, Z.; Saha, B.; Vlachos, D.G. Catalytic hydrotreatment of humins to bio-oil in methanol over supported metal catalysts. *ChemSusChem* **2018**, *11*, 3609–3617. [[CrossRef](#)] [[PubMed](#)]
16. Wang, Y.; Agarwal, S.; Tang, Z.; Heeres, H.J. Exploratory catalyst screening studies on the liquefaction of model humins from C₆ sugars. *RSC Adv.* **2017**, *7*, 5136–5147. [[CrossRef](#)]
17. Sun, J.; Cheng, H.; Zhang, Y.; Zhang, Y.; Lan, X.; Zhang, Y.; Xia, Q.; Ding, D. Catalytic hydrotreatment of humins into cyclic hydrocarbons over solid acid supported metal catalysts in cyclohexane. *J. Energy Chem.* **2021**, *53*, 329–339. [[CrossRef](#)]
18. Summerskii, I.V.; Krutov, S.M.; Zarubin, M.Y. Humins-like substances formed under the conditions of industrial hydrolysis of wood. *Russ. J. Appl. Chem.* **2010**, *83*, 320–327. [[CrossRef](#)]
19. Fergani, M.E.; Candu, N.; Tudorache, M.; Bucur, C.; Djelal, N.; Granger, P.; Coman, S.M. From useless humins by-product to Nb@graphite-like carbon catalysts highly efficient in HMF synthesis. *Appl. Catal. A Gen.* **2021**, *618*, 118130. [[CrossRef](#)]
20. Zandvoort, I.V.; Koers, E.J.; Weingarth, M.; Bruijninx, P.C.A.; Baldus, M.; Weckhuysen, B.M. Structural characterization of ¹³C-enriched humins and alkali-treated ¹³C humins by 2D solid-state NMR. *Green Chem.* **2015**, *17*, 4383–4392. [[CrossRef](#)]
21. Filiciotto, L.; Balu, A.M.; Romero, A.A.; Angelici, C.; Waal, J.C.V.D.; Luque, R. Reconstruction of humins formation mechanism from decomposition products: A GC-MS study based on catalytic continuous flow depolymerizations. *Mol. Catal.* **2019**, *479*, 110564. [[CrossRef](#)]
22. Fodor, D.; Ishikawa, T.; Krumeich, F.; Bokhoven, J.A.V. Synthesis of single crystal nanoreactor materials with multiple catalytic functions by incipient wetness impregnation and ion exchange. *Adv. Mater.* **2015**, *27*, 1919–1923. [[CrossRef](#)]
23. Chai, Y.; Shang, W.; Li, W.; Wu, G.; Dai, W.; Guan, N.; Li, L. Noble metal particles confined in zeolites: Synthesis, characterization, and applications. *Adv. Sci.* **2019**, *6*, 1900299. [[CrossRef](#)]
24. Okumura, K.; Niwa, M. Regulation of the Dispersion of PdO through the interaction with acid sites of zeolite studied by extended X-ray absorption fine structure. *J. Phys. Chem. B* **2000**, *104*, 9670–9675. [[CrossRef](#)]
25. Fergani, M.E.; Candu, N.; Coman, S.M.; Parvulescu, V.I. Nb-Based zeolites: Efficient bi-functional catalysts for the one-pot synthesis of succinic acid from glucose. *Molecules* **2017**, *22*, 2218. [[CrossRef](#)]
26. Beyerlein, R.A.; Choi Feng, C.; Hall, J.B.; Huggins, B.J.; Ray, G.J. Effect of steaming on the defect structure and acid catalysis of protonated zeolites. *Top. Catal.* **1997**, *4*, 27–42. [[CrossRef](#)]
27. Remy, M.J.; Stanica, D.; Poncelet, G.; Feijen, E.J.P.; Grobet, P.J.; Martens, J.A.; Jacobs, P.A. Dealuminated H-Y zeolites: Relation between physicochemical properties and catalytic activity in heptanes and decane isomerization. *J. Phys. Chem.* **1996**, *100*, 12440–12447. [[CrossRef](#)]
28. Jamalzadeh, Z.; Haghighi, M.; Asgari, N. Synthesis, physicochemical characterizations and catalytic performance of Pd/carbon-zeolite and Pd/carbon-CeO₂ nanocatalysts used for total oxidation of xylene at low temperatures. *Front. Environ. Sci. Eng.* **2013**, *7*, 365–381. [[CrossRef](#)]

29. Jablon'ska, M.; Król, A.; Kukulska-Zajac, E.; Tarach, K.; Chmielarz, L.; Góra-Marek, K. Zeolite Y modified with palladium as effective catalyst for selective catalytic oxidation of ammonia to nitrogen. *J. Catal.* **2014**, *316*, 36–46. [CrossRef]
30. Tian, F.; Wu, Y.; Shen, Q.; Li, X.; Chen, Y.; Meng, C. Effect of Si/Al ratio on mesopore formation for zeolite beta via NaOH treatment and the catalytic performance in α -pinene isomerization and benzylation of naphthalene. *Micropor. Mesopor. Mat.* **2013**, *173*, 129–138. [CrossRef]
31. Penner, S.; Wang, D.; Jenewein, B.; Gabasch, H.; Klotzer, B.; Knop-Gericke, A.; Schlogl, B.; Hayek, K. Growth and decomposition of aligned and ordered PdO nanoparticles. *J. Chem. Phys.* **2006**, *125*, 94703. [CrossRef]
32. Fleisch, T.H.; Hicks, R.F.; Bell, A.T. An XPS study of metal-support interactions on PdSiO₂ and PdLa₂O₃. *J. Catal.* **1984**, *87*, 398–413. [CrossRef]
33. Chichova, D.; Mäki-Arvela, P.; Heikkilä, T.; Kumar, N.; Väyrynen, J.; Salmi, T.; Murzin, D.Y. X-ray Photoelectron Spectroscopy Investigation of Pd-Beta Zeolite Catalysts with Different Acidities. *Top. Catal.* **2009**, *52*, 359–379. [CrossRef]
34. Stakheev, A.Y.; Kustov, L.M. Effects of the support on the morphology and electronic properties of supported metal clusters: Modern concepts and progress in 1990s. *Appl. Catal. A Gen.* **1999**, *188*, 3–35. [CrossRef]
35. Klie, R.F.; Browning, N.D.; Chowdhuri, A.R.; Takoudis, C.G. Analysis of ultrathin SiO₂ interface layers in chemical vapor deposition of Al₂O₃ on Si by in situ scanning transmission electron microscopy. *Appl. Phys. Lett.* **2003**, *83*, 1187. [CrossRef]
36. Guillemot, D.; Polisset-Thfoin, M.; Fraissard, J.; Bonnin, D. New Method for Obtaining Palladium Particles on Y Zeolites. Characterization by TEM, ¹²⁹Xe NMR, H₂ Chemisorption, and EXAFS. *J. Phys. Chem. B* **1997**, *101*, 8243–8249. [CrossRef]
37. Wagner, C.D.; Davis, L.E.; Zeller, M.V.; Taylor, J.A.; Raymond, R.H.; Gale, L.H. Empirical atomic sensitivity factors for quantitative analysis by electron spectroscopy for chemical analysis. *Surf. Interface Anal.* **1981**, *3*, 211–225. [CrossRef]
38. Gallagher, P.K.; Gross, M.E. The thermal decomposition of palladium acetate. *J. Therm. Anal.* **1986**, *31*, 1231–1241. [CrossRef]
39. Shen, W.J.; Okumura, M.; Matsumura, Y.; Haruta, M. The influence of the support on the activity and selectivity of Pd in CO hydrogenation. *Appl. Catal. A Gen.* **2001**, *213*, 225–232. [CrossRef]
40. Pieterse, J.A.Z.; Van den Brink, R.W.; Booneveld, S.; de Bruijn, F.A. Influence of zeolite structure on the activity and durability of Co-Pd-zeolite catalysts in the reduction of NO_x with methane. *Appl. Catal. B-Environ.* **2003**, *46*, 239–250. [CrossRef]
41. Chang, T.-C.; Chen, J.-J.; Yeh, C.-T. Temperature-Programmed Reduction and Temperature-Resolved Sorption Studies of Strong Metal-Support Interaction in supported palladium catalysts. *J. Catal.* **1985**, *96*, 51–57. [CrossRef]
42. Byun, M.Y.; Park, D.W.; Lee, M.S. Effect of Oxide Supports on the Activity of Pd Based Catalysts for Furfural Hydrogenation. *Catalysts* **2020**, *10*, 837. [CrossRef]
43. Zheng, Q.; Farrauto, R.; Deeba, M. Part II: Oxidative Thermal Aging of Pd/Al₂O₃ and Pd/Ce_xO_y-ZrO₂ in Automotive Three Way Catalysts: The Effects of Fuel Shutoff and Attempted Fuel Rich Regeneration. *Catalysts* **2015**, *5*, 1797–1814. [CrossRef]
44. Flanigen, E.M.; Khatami, H.; Szymanski, H.A. Infrared Structural Studies of Zeolite Frameworks. In *Molecular Sieve Zeolites, Advances in Chemistry 101*; Flanigen, E.M., Sand, L.B., Eds.; American Chemical Society: Washington, DC, USA, 1971; pp. 201–229. [CrossRef]
45. Banse, B.A.; Koel, B.E. Interaction of oxygen with Pd(111): High effective O₂ pressure conditions by using nitrogen dioxide. *Surf. Sci.* **1990**, *232*, 275–285. [CrossRef]
46. Sacchetto, V.; Gatti, G.; Paul, G.; Braschi, I.; Berlier, G.; Cossi, M.; Marchese, L.; Bagatin, R.; Bisio, C. The interactions of methyl tert-butyl ether on high silicazeolites: A combined experimental and computational study. *Phys. Chem. Chem. Phys.* **2013**, *15*, 13275–13287. [CrossRef]
47. Othman, I.; Mohamed, R.M.; Ibrahim, I.A.; Mohamed, M.M. Synthesis and modification of ZSM-5 with manganese and lanthanum and their effects on decolorization of indigo carmine dye. *Appl. Catal. A-Gen.* **2006**, *299*, 95–102. [CrossRef]
48. Topsøe, N.Y.; Pedersen, K.; Derouane, E.G. Infrared and temperature-programmed desorption study of the acidic properties of ZSM-5-type zeolites. *J. Catal.* **1981**, *70*, 41–52. [CrossRef]
49. Blåkera, C.; Pasel, C.; Luckas, M.; Dreisbach, F.; Bathen, D. Investigation of load-dependent heat of adsorption of alkanes and alkenes on zeolites and activated carbon. *Micropor. Mesopor. Mat.* **2017**, *241*, 1–10. [CrossRef]
50. Zhang, J.; Wang, L.; Zhu, L.; Wu, Q.; Chen, C.; Wang, X.; Ji, Y.; Meng, X.; Xiao, F.S. Solvent-Free Synthesis of Zeolite Crystals Encapsulating Gold-Palladium Nanoparticles for the Selective Oxidation of Bioethanol. *ChemSusChem* **2015**, *8*, 2867–2871. [CrossRef]
51. Panagiotopoulou, P.; Vlachos, D.G. Liquid phase catalytic transfer hydrogenation of furfural over a Ru/C catalyst. *Appl. Catal. A Gen.* **2014**, *480*, 17–24. [CrossRef]
52. Jae, J.; Zheng, W.; Lobo, R.F.; Vlachos, D.G. Production of Dimethylfuran from Hydroxymethylfurfural through Catalytic Transfer Hydrogenation with Ruthenium Supported on Carbon. *ChemSusChem* **2013**, *6*, 1158–1162. [CrossRef]
53. Jongorius, A.L.; Copeland, J.R.; Foo, G.S.; Hofmann, J.P.; Bruijninx, P.C.A.; Sievers, C.; Weckhuysen, B.M. Stability of Pt/ γ -Al₂O₃ catalysts in lignin and lignin model compound solutions under liquid phase reforming reaction conditions. *ACS Catal.* **2013**, *3*, 464–473. [CrossRef]
54. Zeolyst International. Available online: <https://www.zeolyst.com/our-products/standard-zeolite-powders.html> (accessed on 1 June 2021).
55. Teodorescu, C.M.; Esteva, J.M.; Karnatak, R.C.; Afif, A.E. An approximation of the Voigt I profile for the fitting of experimental x-ray absorption data. *Nucl. Instrum. Methods Phys. Res. Sect. A Accel. Spectrom. Dect. Assoc. Equip.* **1994**, *345*, 141–147. [CrossRef]
56. Mardare, D.; Luca, D.; Teodorescu, C.M.; Macovei, D. On the hydrophilicity of nitrogen-doped TiO₂ thin films. *Surf. Sci.* **2007**, *601*, 4515–4520. [CrossRef]